PCCP

PAPER

View Article Online
View Journal | View Issue

Cite this: *Phys. Chem. Chem. Phys.*, 2020, **22**, 2327

Combining experiment and computation to elucidate the optical properties of Ce^{3+} in $Ba_5Si_8O_{21}$†

Jiyou Zhong,[a] Shruti Hariyani,[b] Ya Zhuo,[b] Weiren Zhao,*[a] Xiang Liu,[a] Jun Wen*[c] and Jakoah Brgoch*[b]

Received 12th October 2019,
Accepted 6th January 2020

DOI: 10.1039/c9cp05576b

rsc.li/pccp

Complex alkaline earth silicates have been extensively studied as rare-earth substituted phosphor hosts for use in solid-state lighting. One of the biggest challenges facing the development of new phosphors is understanding the relationship between the observed optical properties and the crystal structure. Fortunately, recent improvements in characterization techniques combined with advances in computational methodologies provide the research tools necessary to conduct a comprehensive analysis of these systems. In this work, a new Ce^{3+} substituted phosphor is developed using $Ba_5Si_8O_{21}$ as the host crystal structure. The compound is evaluated using a combination of experimental and computational methods and shows $Ba_5Si_8O_{21}$:Ce^{3+} adopts a monoclinic crystal structure that was confirmed through Rietveld refinement of high-resolution synchrotron powder X-ray diffraction data. Photoluminescence spectroscopy reveals a broad-band blue emission centered at ~440 nm with an absolute quantum yield of ~45% under ultraviolet light excitation (λ_{ex} = 340 nm). This phosphor also shows a minimal chromaticity-drift but with moderate thermal quenching of the emission peak at elevated temperatures. The modest optical response of this phase is believed to stem from a combination of intrinsic structural complexity and the formation of defects because of the aliovalent rare-earth substitution. Finally, computational modeling provides essential insight into the site preference and energy level distribution of Ce^{3+} in this compound. These results highlight the importance of using experiment and computation in tandem to interpret the relationship between observed optical properties and the crystal structures of all rare-earth substituted complex phosphors.

Introduction

Phosphor-converted white light emitting diodes (pc-LEDs) are quickly becoming the ubiquitous source of lighting in daily life due to their potential significant energy-savings, long operating lifetimes, and environmentally friendly compositions.[1–3] These bulbs create white light from a monochromatic LED by down-converting the emission using one or more rare-earth substituted inorganic phosphors.[4–6] Depending on the emission wavelength of the LED, which can range from the near-UV (365–400 nm) to the blue region of the electromagnetic spectrum (430–470 nm), different phosphors are required.[6–8] Many strategies can be used when choosing new phosphor hosts, such as searching through crystal structure databases, preparing co-substitutions, or forming solid solutions.[9–11] These approaches have led to the discovery of many new phosphors over the past several years with a wide range of optical properties, many with potential applications in general lighting or display technology. Interestingly, when analyzing the compositions of current commercial phosphors, many of these compounds are silicon containing hosts, including oxides, nitrides, and oxynitrides. For example, yellow-emitting $La_3Si_6N_{11}$:Ce^{3+} and Sr_2SiO_4:Eu^{2+}, green-emitting β-SiAlON:Eu^{2+}, Ba_2SiO_4:Eu^{2+}, and $Ba_3Si_6O_{12}N_2$:Eu^{2+}, and red-emitting $Sr_2Si_5N_8$:Eu^{2+} and $CaAlSiN_3$:Eu^{2+} have all been successfully incorporated in pc-LEDs due to their excellent photoluminescent properties and thermal stability.[12–17] Therefore, silicon-based compounds might be considered prime candidates when searching for new promising phosphor hosts.

Silicon-containing compounds, specifically complex alkaline-earth silicates, have been widely investigated due to their structural versatility, ease of luminescent ion incorporation, and wide availability of inexpensive raw materials.[18,19] In particular, ternary barium silicates, with superior structural stability, chemical stability,

[a] *School of Physics and Optoelectronic Engineering, Guangdong University of Technology, Guangzhou 510006, China. E-mail: zwren123@126.com*
[b] *Department of Chemistry, University of Houston, Houston, Texas 77204, USA. E-mail: jbrgoch@uh.edu*
[c] *School of Physics and Electronic Engineering, Anqing Normal University, Anqing 246133, China. E-mail: wenjunkd@mail.ustc.edu.cn*

† Electronic supplementary information (ESI) available. See DOI: 10.1039/c9cp05576b

and a clear substitution site, show outstanding potential as practical phosphors. Examining the compounds reported in the BaO–SiO_2 phase space reveals that several stable phases can form, including Ba_3SiO_5, Ba_2SiO_4, $BaSiO_3$, $Ba_2Si_3O_8$, $Ba_5Si_8O_{21}$, $Ba_3Si_5O_{13}$, and $BaSi_2O_5$.[20–22] These compounds show a wide range of luminescent properties upon substituting Ba^{2+} with Eu^{2+} including the resulting emission varying from blue to orange depending on the chemical composition and crystal structure.[23–30] However, there is significantly less research on the luminescent properties of Ce^{3+} substituted barium silicate phosphors. One possible reason is that incorporating Ce^{3+} for the Ba^{2+} site is an aliovalent substitution, which inherently causes the formation of crystal defects. Generally, a high concentration of defects in the host crystal structure is harmful to luminescence efficiency as defects can act as a quenching center.[31] However, this does not necessarily mean all Ce^{3+} activated barium silicates possess low efficiencies. Ba_2SiO_4:Ce^{3+} exhibits a photoluminescent quantum yield (PLQY) as high as 66%.[32] Research has also indicated that a reasonably small amount of crystal defects play a considerable role in reducing thermal quenching through possible energy transfer from defects to luminescence centers.[33,34]

In this work, we present a Ce^{3+}-substituted $Ba_5Si_8O_{21}$ blue-emitting phosphor prepared *via* high temperature solid-state synthesis. A detailed crystal structure, electronic structure, and optical property analysis was conducted. Additionally, computational analysis of the Ce^{3+} site preference and calculation on the 4f ↔ 5d transitions of each site were performed to understand the relationship between the observed optical properties and the crystal structure. This study not only produces an interesting silicon-based luminescent material, but the work also highlights computational quantum mechanics as a method to gain a better understanding of complex inorganic phosphors.

Methodology

Synthesis

$(Ba_{0.95}Ce_{0.05})_5Si_8O_{21}$ was prepared by high-temperature solid-state synthesis using $BaCO_3$ (Sigma-Aldrich, 99.95%), SiO_2 (Aldrich, 99.95%) and CeO_2 (Aldrich, 99.995%) as the starting materials. The raw materials were first dried at 673 K for 24 h before being weighed according to the required stoichiometric ratio. The resulting mixture was then finely ground for 1 hour using an agate mortar and pestle and then placed in a graphite crucible. The powder was heated at 1523 K for 8 hours under a flowing reducing atmosphere (5% H_2/95% N_2) using a heating and cooling rate of 3 K min^{-1}. The final product was finally ground into a fine powder using an agate mortar and pestle.

Characterization

The synchrotron X-ray powder diffraction data were collected at 298 K using the 11-BM at the Advanced Photon Source (APS) at Argonne National Laboratory, with a calibrated wavelength of 0.412835 Å. The room temperature and temperature-dependent photoluminescent spectra were recorded using a PTI QuantaMaster with a 75 W xenon arc lamp for excitation and a Janis cryostat (VPF-100) to control the temperature between 80 and 500 K. The internal PLQY was measured at room temperature using a 150 mm Spectralon™-coated integrating sphere following the method of de Mello *et al.*[35] The time-gated photoluminescence decay measurements were collected using a Horiba DeltaFlex Lifetime System. The thermoluminescence (TL) curves were collected by a thermoluminescence meter (SL08-L, Guangzhou-Radiation Science and Technology Co. Ltd) with the heating rate of 1 K s^{-1} after being excited for 10 min. The scanning electron microscopy (SEM) images and energy dispersive spectrum (EDS) mapping were measured on a Hitachi-S4800 (Japan). Inductively coupled plasma (ICP) test was carried out on a Agilent 7700 ICP-MS system (USA). The X-ray photoelectron spectroscopy (XPS) was measured on ESCALAB 250Xi (Thermo Fisher), using the Al Kα line as an X-ray source with a minimum resolution of 0.45 eV (Ag $3d_{5/2}$). The Rietveld profile refinement was performed with the General Structure Analysis System (GSAS) software and the EXPGUI interface.[36]

Computational modeling

The Ce-substituted $Ba_5Si_8O_{21}$ crystal structure was modeled using a unit cell containing 136 atoms, in which one Ba^{2+} ion was substituted with a Ce^{3+} ion, corresponding to doping concentration of 5%. To simulate a potential neutral, charge compensated model and minimize structural distortion, a Si^{4+} ion was replaced with an Al^{3+} ion at a remote distance. Structural optimization, electronic properties, and defect formation energy calculations were carried out following density functional theory (DFT) calculations using the PBE exchange–correlation functional, as well as the HSE06 and PBE0 hybrid functionals, as implemented in the Vienna *ab initio* Simulation Package (VASP).[37–41] The geometric structures were fully relaxed with an electronic convergence criterion of 1×10^{-5} eV and convergence criterion of 0.01 eV $Å^{-1}$ for the Hellman–Feynman forces on the atoms. A cutoff energy of 500 eV was used for the basis set of the plane waves, and a $1 \times 5 \times 3$ Γ-centered Monkhorst–Pack k-point grid was used to sample the first Brillouin zone.

The energies and relative oscillator strengths of the 4f ↔ 5d transitions of Ce^{3+} ions were calculated based on the optimized crystal structures, composed of Ce^{3+}-centered defect clusters, *i.e.*, $(CeO_6)^{9-}$ and $(CeO_8)^{13-}$, embedded into the $Ba_5Si_8O_{21}$ host. Then, wave function-based embedded cluster *ab initio* calculations, as implemented in the MOLCAS program,[42] were performed. The accurate quantum chemical *ab initio* calculations were used to treat the valence electrons of the atoms in the defect clusters, whose immediate lattice environments were represented by the embedding *ab initio* model potentials (AIMPs) located at the host lattice sites within a sphere of radius 10.0 Å.[43] Point charges were then situated at lattice sites within a sphere of the radius 50.0 Å to represent the lattice environments outside of the AIMPs. The CASSCF/CASPT2/RASSI-SO methods utilized in the embedded cluster calculations also include the effects of the spin–orbit coupling and second-order perturbation correction,[44,45] and thus, give the

energies and wavefunctions of the 4f and 5d states for the Ce^{3+} ion.[46,47]

Results and discussion

Synthesis, morphology, crystal and electronic structure description

$Ba_5Si_8O_{21}$ has previously been reported as an excellent persistent luminescent phosphor when substituted with Eu^{2+}.[29] According to the reports,[29,48–50] $Ba_5Si_8O_{21}$ can be obtained through heating $BaCO_3$ and SiO_2 in a 5 : 8 atomic ratio at 1523 K for 10 hours. However, numerous attempts to follow these reaction conditions, including adjusting the reaction temperature, adding flux, multistep sintering, and pressing a pellet of the raw powder before heating all failed to achieve a pure phase product. In each attempt, a multi-phase product with $Ba_4Si_6O_{16}$ and $BaSi_2O_5$ was obtained due to this rich ternary phase space having nearly identical reaction conditions for all of the phases. The only approach to obtain single-phase $Ba_5Si_8O_{21}$ is by controlling the Ba/Si ratio exactly by thoroughly drying starting materials and then meticulously adjusting the Ba/Si ratio and scrutinizing the powder X-ray diffractograms of each product for any impurities. Following this tedious synthesis, the title phase was ultimately achieved as a highly crystalline, phase pure product as confirmed by high-resolution synchrotron X-ray diffraction. The final Rietveld refinement is shown in Fig. 1a where the published $Ba_5Si_8O_{21}$ crystal structure was employed as the initial model.[51] Ce^{3+} was omitted in the refinement owing to the low (5 mol%) substitution concentration. The refinement details and refined atomic positions are provided in Tables 1 and 2, respectively. The refinement exhibited excellent agreement between the collected data and the structural model, which proves the product's excellent phase purity.

The morphology of the sample $(Ba_{0.95}Ce_{0.05})_5Si_8O_{21}$ was checked by scanning electron microscope (SEM) (shown as Fig. 2a), indicating the particles are irregular in shape with a size of 10–20 μm. To examine the elemental distribution and composition of the synthesized sample, $(Ba_{0.95}Ce_{0.05})_5Si_8O_{21}$, energy dispersive spectroscopy (EDS) was used to map the location of the elements. As shown in Fig. 2b–e, the product contains only Ba, Si, O, and Ce and the elements are uniformly distributed in the particles examined. Furthermore, inductively coupled plasma (ICP) was used to determine the exact Ce concentration with the result (show in the inset of Fig. 2f), indicating the Ce concentration is about 4 mol%, which is in good agreement with the 5 mol% loaded. X-ray photoelectron spectroscopy (XPS) was adopted to analyze the valence state of Ce in $(Ba_{0.95}Ce_{0.05})_5Si_8O_{21}$. The resulting spectrum, plotted in Fig. 3, demonstrated the expected +3 valence state for Ce in this compound.

$Ba_5Si_8O_{21}$ crystallizes in the monoclinic crystal system with space group $C2/c$ (no. 15).[51] The crystal structure, illustrated in Fig. 1b, is a combination of multiple barium centered polyhedral units and $[SiO_4]$ tetrahedral units. The $[SiO_4]$ tetrahedra

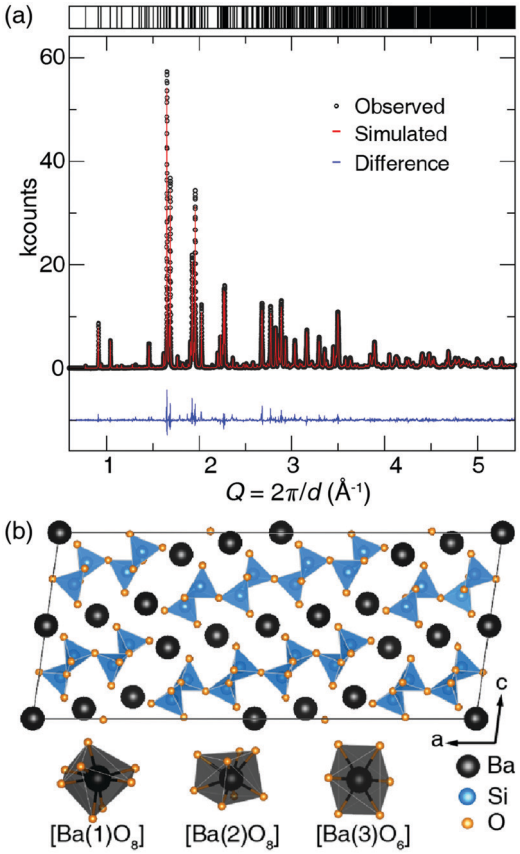

Fig. 1 (a) Rietveld refinement of high-resolution synchrotron X-ray diffraction of $(Ba_{0.95}Ce_{0.05})_5Si_8O_{21}$. The measured data are represented by black circles, the refinement fit is in red, and the difference curve is in blue; (b) the crystal structure of $Ba_5Si_8O_{21}$ and coordination environment of each Ba^{2+} ion.

Table 1 Rietveld refinement and crystal data for $(Ba_{0.95}Ce_{0.05})_5Si_8O_{21}$

Formula	$Ba_5Si_8O_{21}$
Radiation type; λ (Å)	Synchrotron; 0.412835
Q range (Å^{-1})	0.500–5.500
Temperature (K)	298
Space group; Z	$C2/c$; 4
a (Å)	32.66762(2)
b (Å)	4.69999(7)
c (Å)	13.87231(5)
β (deg)	98.22(9)
Unit cell volume (Å^3)	2107.99(5)
Profile R-factor, R_p	0.1023
Weighted profile R-factor, R_{wp}	0.1383

are corner connected, forming a *Zweier* single-chain that extends in the *ac*-plane. The barium ions are inserted into the interstitial voids between *Zweier* single-chains, generating three crystallographically independent sites. Ba(1) is surrounded by eight oxygen atoms with Ba–O distances ranging from 2.6859(7) to 2.9859(3) Å, presenting a centrosymmetric square prism $[Ba(1)O_8]$ with slight site distortion. Ba(2) is also eight-coordinated with Ba–O distances ranging from 2.649(9) to 3.0936(5) Å, forming a highly distorted $[Ba(2)O_8]$ polyhedron. Ba(3) is six-coordinated with Ba–O distances ranging from 2.7836(6) to 2.8578(9) Å and exhibits a slightly

Table 2 The refined atomic positions for $Ba_5Si_8O_{21}$

Atom	Wyck. position	Occ.	x	y	z	U_{iso}
Ba(1)	8f	1	0.2184(6)	0.007(6)	0.3823(8)	0.0161(1)
Ba(2)	8f	1	0.3877(2)	0.0003(4)	0.0537(6)	0.0195(2)
Ba(3)	4a	1	0	0	0	0.0038(7)
Si(1)	8f	1	0.1908(8)	0.0351(5)	0.1024(9)	0.0051(6)
Si(2)	8f	1	0.3350(7)	0.0150(4)	0.2864(4)	0.0278(3)
Si(3)	8f	1	0.4268(9)	0.0683(7)	0.3421(4)	0.0220(8)
Si(4)	8f	1	0.0487(8)	−0.0681(9)	0.27(4)	0.0191(9)
O(1)	8f	1	0.2410(7)	−0.0111(7)	0.0780(5)	0.01(1)
O(2)	8f	1	0.1591(8)	−0.0336(4)	0.5034(7)	0.01(1)
O(3)	8f	1	0.199(5)	0.3246(1)	0.1609(7)	0.01(1)
O(4)	8f	1	0.325(4)	0.3399(1)	0.3140(8)	0.01(1)
O(5)	8f	1	0.3331(3)	0.009(1)	0.1758(5)	0.01(1)
O(6)	8f	1	0.3825(5)	−0.0085(2)	0.3491(4)	0.01(1)
O(7)	8f	1	0.0422(6)	0.4709(5)	0.0659(8)	0.01(1)
O(8)	8f	1	0.4308(4)	0.4346(8)	0.3006(8)	0.01(1)
O(9)	8f	1	0.0585(1)	0.3885(6)	0.2619(2)	0.01(1)
O(10)	8f	1	0.4352(8)	0.5416(1)	0.1119(4)	0.01(1)
O(11)	4e	1	0	0.1166(1)	1/4	0.01(1)

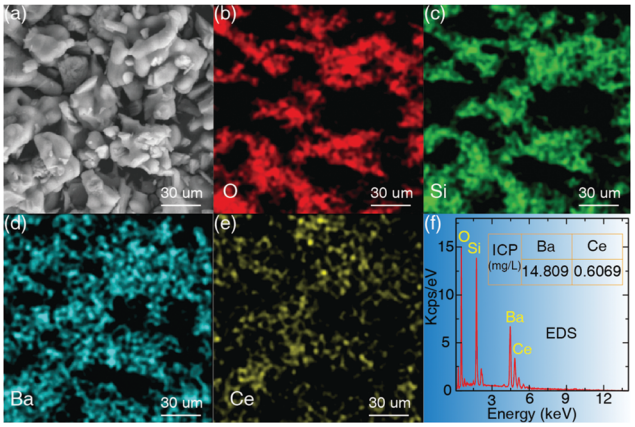

Fig. 2 (a) Scanning electron microscopy (SEM) image; and energy dispersive spectrum (EDS) mapping of element (b) O, (c) Si, (d) Ba, and (e) Ce; (f) EDS survey of randomly selected point, inset is the measured result of Ba^{2+} and Ce^{3+} ion concentration in an acid solution dissolved the sample $(Ba_{0.95}Ce_{0.05})_5Si_8O_{21}$.

distorted $[Ba(3)O_6]$ octahedron. Considering the ionic radii of the constituent atoms, it is only possible for Ce^{3+} to substitute on the Ba^{2+} sites; however, it is not clear which specific Ba site is preferred by Ce^{3+} and it is hard to refine the rare-earth occupancy, even using synchrotron diffraction, due to the complex crystal structure and multiple potential substitution sites.

To gain a better understanding of $Ba_5Si_8O_{21}$, electronic structure calculations were conducted. The electronic band structure of $Ba_5Si_8O_{21}$ was calculated using the PBE functional and is illustrated in Fig. 4a. This compound has a direct band gap ($E_{g,PBE}$) of 4.5 eV at the Γ point, which is expected to be underestimated because of the inherent shortcomings of the PBE method. This value of the band gap is much larger than that of Ba_3SiO_5 (3.04 eV) and $BaSi_2O_5$ (3.2 eV),[52,53] which were also calculated at the PBE-level. However, because PBE is known to underestimate the band gap, a hybrid functional

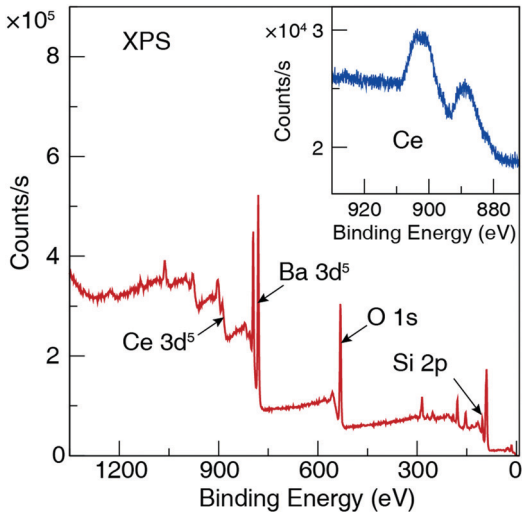

Fig. 3 X-ray photoelectron spectroscopy (XPS) survey of $(Ba_{0.95}Ce_{0.05})_5Si_8O_{21}$ with the inset highlighting Ce 3d in this sample.

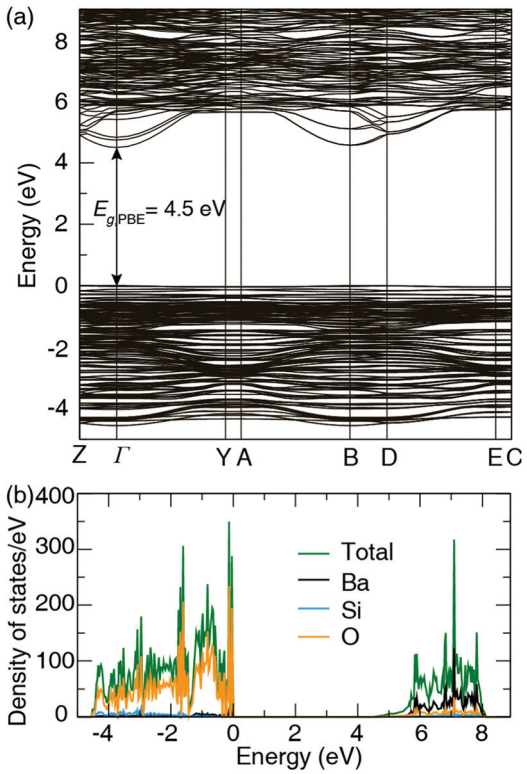

Fig. 4 (a) Band structure and (b) density of states of $Ba_5Si_8O_{21}$ calculated using the PBE functional.

(HSE06) was used to calculate the band gap which gave a value of $E_{g,HSE06}$ = 6.0 eV (Fig. S1, ESI†). Decomposing the electronic structure into the partial density of states, as shown in Fig. 4b, indicates the O 2p states set the top of the valence band. In contrast, the bottom of the conduction band is determined by unoccupied Ba 5d states with relatively strong hybridization between the O 2p and Ba 5d in the conduction band. Interestingly the contribution of Si 3p and 3s states in conduction and

valence band are very weak. The results of electronic properties investigation suggest that $Ba_5Si_8O_{21}$ presents typical electronic configuration and has a sufficient band gap width, making it a promising phosphor host.

Photoluminescence properties of Ce^{3+} in $Ba_5Si_8O_{21}$

Substituting Ce^{3+} for Ba^{2+} in $Ba_5Si_8O_{21}$ produces a photoluminescence spectrum from the rare-earth's 4f ↔ 5d electronic transitions, shown in Fig. 5. Measuring the room temperature (298 K) photoluminescent excitation and emission of $Ba_5Si_8O_{21}$:Ce^{3+} reveals a broad excitation band covering 230 nm to 390 nm with two excitation peaks located at approximately 290 nm and 340 nm. The emission spectrum produced when this material is excited at 340 nm shows an asymmetric emission band ranging from 360 nm to 650 nm with the peak centered at ~440 nm. The photoluminescent quantum yield was measured to be 45% under 340 nm excitation, which is lower than that of Ba_2SiO_4:Ce^{3+} (66%) but higher than that of $Ba_4Si_6O_{16}$:Ce^{3+} (35.9%).[18,32] It is possible the quantum yield of this phase may be somewhat higher as the rare-earth concentration could not be optimized given the difficulty in obtaining pure phase products in this composition space. The full width at half maximum (FWHM) was determined to be 125 nm (6028 cm^{-1}). This compound has three different crystallographic sites for Ce^{3+} to occupy and the 4f orbitals of Ce^{3+} have two ground states corresponding to the spin–orbit coupled $^2D_{3/2}$ → $^2F_{5/2}$ and $^2D_{3/2}$ → $^2F_{7/2}$ transitions,[54,55] resulting in a complicated, multi-component emission spectrum. Attempts to deconvolute the emission data by fitting it with multiple Gaussian curves showed that three Gaussian peaks (centering at 410, 449, and 505 nm, respectively) could perfectly describe the data, presenting consistent with three distinct emission centers. The hypothesis of multiple site occupancy is further supported by monitoring the excitation spectrum at different emission wavelengths. Fig. 6a presents the two observed excitation peaks with the relative intensity of lower energy peak gradually becoming more intense as the monitored emission wavelength increases. The emission spectrum when excited at different wavelengths, depicted in Fig. 6b, shows that the emission slightly red-shifts with increasing excitation wavelength. Interestingly, the emission spectrum when excited by 290 nm presents a shoulder at ~360 nm, and the excitation spectrum monitored at 360 nm exhibits a characteristic 8-coordinated Ce^{3+} emission with two peaks located at 240 nm and 290 nm, respectively. These results indicate that the luminescent center with lower energy excitation generates lower energy emission and that energy transfer from a higher energy luminescent center to a lower energy luminescent center may occur. Despite this spectral analysis, a luminescent center cannot confidently be assigned to a corresponding crystal site.

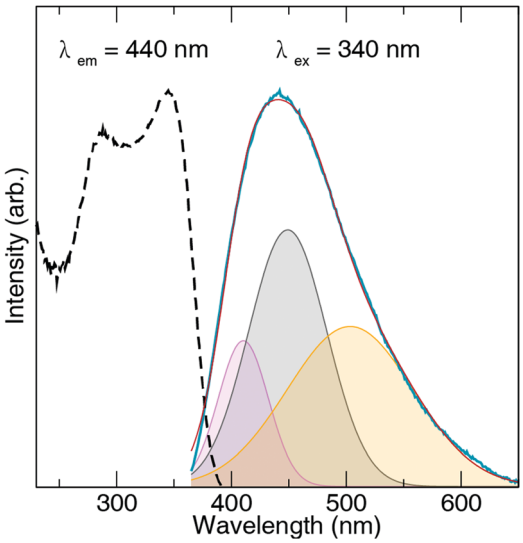

Fig. 5 Photoluminescent excitation and emission spectra of $(Ba_{0.95}Ce_{0.05})_5Si_8O_{21}$ at room temperature. The emission spectra is well fitted (red curve) to present three Gaussian bands (violet, gray and orange) characteristic of Ce^{3+}.

To gain more insight into the site occupation of Ce^{3+}, the room temperature time-gated photoluminescence decay curves (Fig. 7) of $Ba_5Si_8O_{21}$:Ce^{3+} were collected under 330 nm and 360 nm excitation, respectively. Both of the curves can be well fitted by a tri-exponential function following eqn (1):[56,57]

$$I = A + A_1 \exp\left(\frac{-t}{\tau_1}\right) + A_2 \exp\left(\frac{-t}{\tau_2}\right) + A_3 \exp\left(\frac{-t}{\tau_3}\right) \quad (1)$$

where I is intensity, A, A_1, A_2 and A_3 are pre-exponential constants, τ_1, τ_2 and τ_3 are decay times for the exponential components in ns, and t is the measured time. The fitted parameters are listed in Table 3, using an excitation wavelength of 330 nm and 360 nm excitation with the resulting average luminescent lifetime determined using eqn (2) to be 40.4 ns and 44.5 ns, respectively.[58] This lifetime is noticeably shorter than that of well-known YAG:Ce^{3+} (60 ns) despite similar Ce^{3+} doping concentrations mainly due to the non-radiative relaxation consuming energy.[59]

$$\tau = \frac{A_1\tau_1^2 + A_2\tau_2^2 + A_3\tau_3^2}{A_1\tau_1 + A_2\tau_2 + A_3\tau_3} \quad (2)$$

These results support that the emission is stemming from the rare-earth occupying the three distinct luminescent centers, and further indicates that different excitations wavelength may excite the different luminescent centers at different degrees, which agrees with the reported spectral analysis.

Finally, evaluating the practicality of incorporating $Ba_5Si_8O_{21}$:Ce^{3+} into a lighting device further requires collecting the temperature-dependent emission spectra of $Ba_5Si_8O_{21}$:Ce^{3+} between 80 K and 500 K using 340 nm excitation. As shown in Fig. 8a, the relative emission intensity was nearly constant from 80 K up to 280 K. Further increasing the temperature showed a decrease in the emission intensity up to 500 K. The thermal quenching temperature (T_{50}) of this phosphor, or the temperature at which the emission intensity decreases to 50% of the initial value, is ~360 K. However, if setting the initial temperature to room temperature, the T_{50} of the reported phosphor

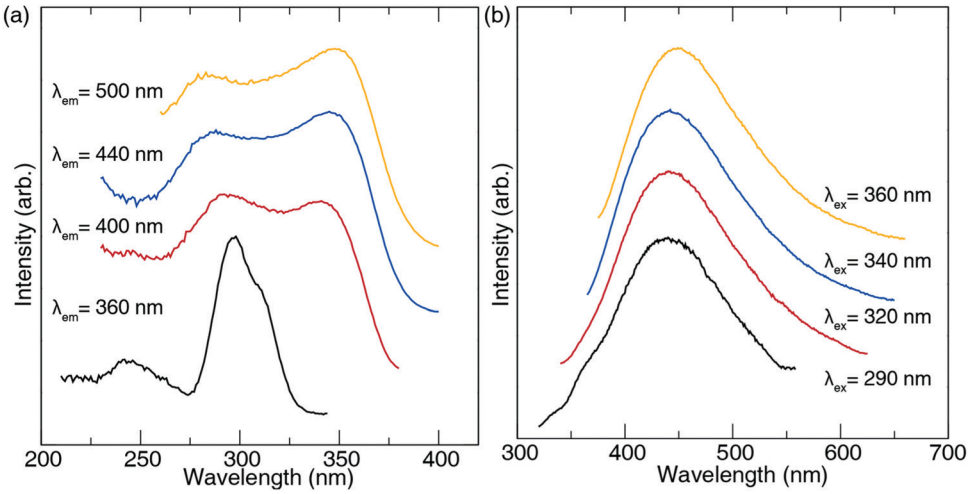

Fig. 6 (a) The excitation spectra of $(Ba_{0.95}Ce_{0.05})_5Si_8O_{21}$ monitored at different emission wavelengths; (b) the emission spectra excited by different excitation wavelengths.

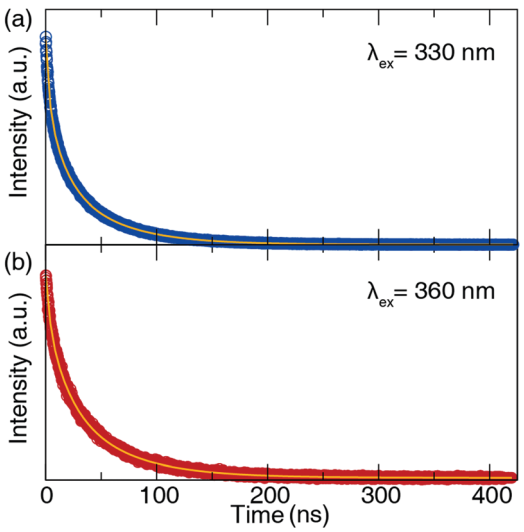

Fig. 7 Time-gated photoluminescence decay curves of $(Ba_{0.95}Ce_{0.05})_5Si_8O_{21}$ collected under (a) 330 nm, and (b) 360 nm excitation, respectively. The blue and red dots represent the collected data and the yellow line is the fit.

Table 3 The parameters of decay curve fitted by a tri-exponential function

Excitation	A	A_1	A_2	A_3	τ_1	τ_2	τ_3
330 nm	9.26	3481.43	4600.84	5110.60	2.67	14.45	48.75
360 nm	2.35	727.04	1306.72	1649.05	3.54	18.59	52.93

falls closer to the preferable range for device incorporation ($T_{50} \geq 423$ K).[60]

Although the emission intensity drops at elevated temperatures, interestingly, the normalized emission peaks overlap across the entire measured temperature range, indicating no changes are generated in the peak shape or position of emission spectrum as a function of temperature. The normalized emission spectra (Fig. 8b) across the entire temperature range perfectly overlap. This results in minimal chromaticity-drift of this phosphor as a function of temperature, which is rare and very surprising considering this system contains multiple crystallographically independent luminescent centers. The reason for this phenomenon is most likely a stable local structure that maintains a constant crystal field upon increasing temperature, which allows the emission peak position to remain unchanged. Additionally, the emission degradation of each luminescent center should be of the same degree to maintain an unchanged peak shape. For most multi-site phosphor systems, the optical response of the luminescent center behaves differently as a function of temperature; thus, the overall emission spectrum can change as a function of temperature. Contrarily, $Ba_5Si_8O_{21}:Ce^{3+}$ exhibits a negligible change even up to high temperature, which demonstrates a robust ability to maintain its emission color with CIE coordinates of (0.19, 0.20), as illustrated in Fig. 9.

One of the possible sources affecting the temperature-dependent optical properties is the presence of defects. To confirm their presence, thermoluminescence measurements (Fig. 10) on $Ba_5Si_8O_{21}:Ce^{3+}$ were conducted in the temperature range of 320–750 K after irradiating the sample for 10 min at 254 nm. The thermoluminescence curve can be decomposed into four Gaussian bands with peaks located at 354 K, 436 K, 489 K, and 583 K, corresponding to a trap depth energy of 0.71 eV, 0.87 eV, 0.98 eV, 1.17 eV, respectively. The trap depth energies were determined according to the approximate relationship $E_T = T/500$ eV,[61] where T is the temperature in Kelvin. The shallow defect with trap depth energy of 0.71 eV is derived from host material, which shows agreement with the previous report,[29] while substituting Ce^{3+} for Ba^{2+} causes the other three types of defects. However, the thermoluminescence intensity of this phosphor is very intense, which alludes to a high concentration of defects and likely results in the relatively low emission efficiency of this material.

Calculating the 4f → 5d transitions in $Ba_5Si_8O_{21}:Ce^{3+}$

To identify the luminescent centers and investigate the relationship between spectroscopic properties and local structures,

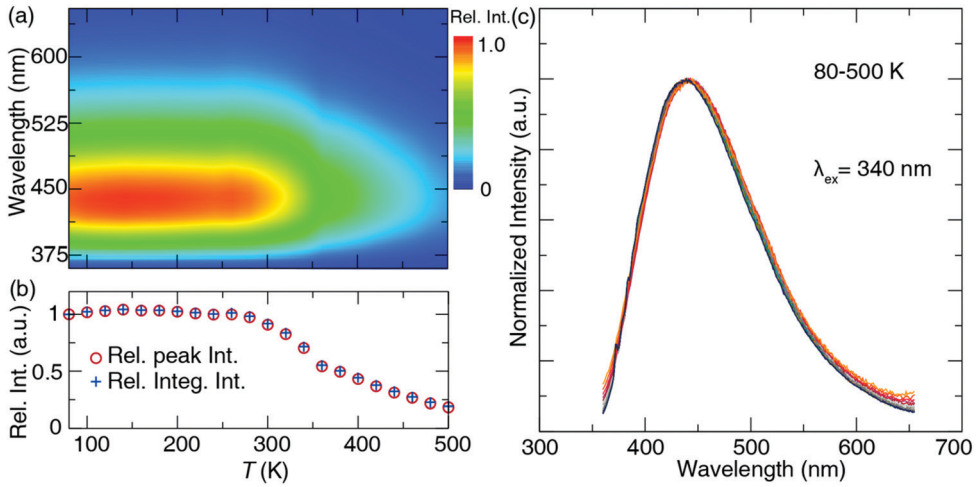

Fig. 8 (a) Contour plot of the normalized emission spectra of $(Ba_{0.95}Ce_{0.05})_5Si_8O_{21}$ excited at 340 nm as a function of temperature; (b) relative integrated intensity of the emission spectra (rel. integ. int.) and the relative intensity of the emission peak (rel. peak int.) as a function of temperature; and (c) all normalized emission spectra of $(Ba_{0.95}Ce_{0.05})_5Si_8O_{21}$ measured between 80 and 500 K.

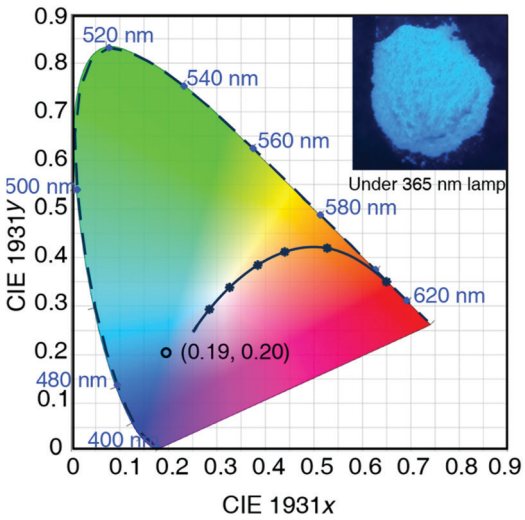

Fig. 9 CIE coordinates of $(Ba_{0.95}Ce_{0.05})_5Si_8O_{21}$ when excited at 340 nm; the inset presents a photograph of this phosphor under a 365 nm lamp.

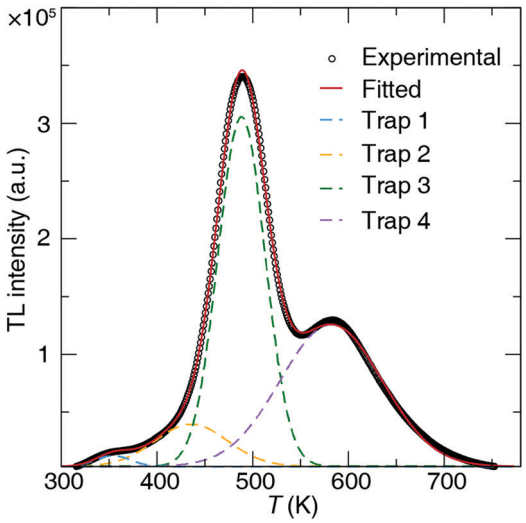

Fig. 10 Thermoluminescence curve of $(Ba_{0.95}Ce_{0.05})_5Si_8O_{21}$ collected from 320 K to 750 K with a heating rate of 1 K s^{-1} after being excited (λ_{ex} = 254 nm) for 10 min.

wave-function-based CASSCF/CASPT2 calculations at the spin–orbit level were performed on Ce-centered embedded clusters to simulate the 4f ↔ 5d transitions. These calculations depend on a reasonably optimized structure model; however, because substituting Ce^{3+} for Ba^{2+} is an aliovalent substitution, charge compensation must be considered to generate neutral defects. There is no unique approach to balance the charge, making it necessary to examine several independent models. In this work, Si^{4+} was replaced with Al^{3+} at a remote distance to minimize structural variations induced by charge compensators. As a result, the local structural variations around Ce^{3+} can only be ascribed to the substituted Ce^{3+} ion. Based on the optimized models, we attempted to obtain the energy difference in Ce doped systems through electronic structure calculations using PBE0 hybrid functional (shown as Fig. S2, ESI†) to identify the emission centers. However, it is hard to find the difference between different doping models. Therefore, we adopted wave function-based embedded cluster *ab initio* calculations to simulate the 4f ↔ 5d transitions, which is more sensitive to the local structures. The calculated 4f ↔ 5d transitions of Ce^{3+} in this defect model were compared with the experimental room temperature excitation spectra monitored at 440 nm, plotted in Fig. 11. The detailed 4f and 5d energy level distributions are presented in Table 4. This calculation indicates that the 4f ↔ 5d transition energies of Ce^{3+} at different Ba^{2+} sites exhibit significant differences depending on the coordination number, bond length, and site distortion. As shown, the calculated centroids (ΔE_{ced}) of the 5d energy levels of the Ce^{3+} ions are slightly changed at different sites, while the crystal-field splitting (ΔE_{cfs}) of each site is severely affected by the local structure. Specifically, the Ce^{3+} on the Ba(2) site presents much

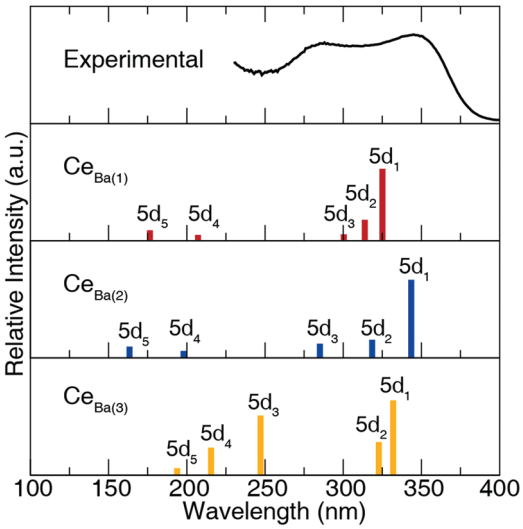

Fig. 11 Schematic of the calculated energy and relative oscillator strengths of 4f ↔ 5d transitions of Ce^{3+} substituted on the different Ba^{2+} sites present in $Ba_5Si_8O_{21}$, compared with the experimental excitation spectra.

larger ΔE_{ced} and ΔE_{cfs} than those on the other two sites mainly due to the lower symmetry and larger distortion of Ba(2) site. This directly leads to the theoretical lowest energy excitation peak of $Ce_{Ba(2)}$ at ~343 nm, which is very close to the experimental excitation observed at 345 nm, enabling this material to be excited by near-ultraviolet light. The simulated 4f ↔ 5d transitions can be incorporated into the experimental excitation band, while the intensity of the higher energy excitation band appears to be inconsistent with the experimental data. This can be ascribed to the Ce^{3+} in this compound having a site preference, and each site may present different concentration quenching properties. The site preference of Ce^{3+} can be evaluated from calculated total free energy (Table 5). The lowest total energy model occurs when Ce occupies the octahedral Ba(3) position while the energies of Ce substituting for Ba on the other two sites is +49 meV ($Ce_{Ba(1)}$) and +334 meV ($Ce_{Ba(2)}$) higher than the lowest energy model. However, the total energies are all relatively similar (the difference is within 0.4 eV), which at the high synthesis temperature of 1523 K (corresponding to an energy barrier of ~3.0 eV) suggests there should not be a strong energetic site preference for Ce substitution. Thus, the shape of the excitation spectrum is more likely to be determined by the difference in the concentration quenching properties of Ce^{3+} on different sites.

Table 4 Calculated energies of the $4f^1$ and $5d^1$ levels for Ce^{3+} ions in the $Ba_5Si_8O_{21}$ host using wave function-based embedded cluster *ab initio* calculations

Levels	$(Ce_{Ba(1)}O_8)^{13-}$ (cm^{-1})	$(Ce_{Ba(2)}O_8)^{13-}$ (cm^{-1})	$(Ce_{Ba(3)}O_6)^{9-}$ (cm^{-1})
$4f_1$	0	0	0
$4f_2$	417	946	391
$4f_3$	1385	1820	1214
$4f_4$	2259	2430	2247
$4f_5$	2581	3046	2537
$4f_6$	3273	3866	3124
$4f_7$	4097	4627	3686
$5d_1$	30 758	29110	30128
$5d_2$	31 873	31 392	30 978
$5d_3$	33 287	35 075	40 465
$5d_4$	48 265	50 534	46 400
$5d_5$	56 667	61 191	51 592
ΔE_{ced}	40 170	41 460	39 913
ΔE_{cfs}	25 909	32 081	21 464

Table 5 PBE-calculated total energies of supercells for Ce^{3+} ions in $Ba_5Si_8O_{21}$ host relative to the lowest energy model

Site	$Ce_{Ba(1)}$	$Ce_{Ba(2)}$	$Ce_{Ba(3)}$
E_{tot} (eV)	+0.049	+0.334	0

Conclusions

In summary, the Ce^{3+} substituted silicate $Ba_5Si_8O_{21}$ was selected from the BaO–SiO_2 binary phase diagram and prepared using conventional high-temperature solid-state synthesis. Past research has shown that silicates are promising hosts for new phosphors materials and subsequently, our optical spectroscopy study indicates that $Ba_5Si_8O_{21}$:Ce^{3+} can be efficiently excited by 340 nm light and exhibits broad-band blue emission with a photoluminescent quantum yield of 45%. The emission was confirmed to stem from three different luminescent centers through spectroscopic analysis, computational modeling of the 4f ↔ 5d transitions, and time-gated photoluminescence decay measurements. Analysis of the temperature-dependent emission revealed that $Ba_5Si_8O_{21}$:Ce^{3+} quenches at elevated temperature, but shows negligible chromatic drift as a function of temperature. The work performed here provides a full evaluation of a new $Ba_5Si_8O_{21}$:Ce^{3+} phosphor through a combination of experimental and theoretical investigation that is useful to further optical materials design.

Conflicts of interest

There are no conflicts to declare.

Acknowledgements

The authors thank the National Natural Science Foundation of China (No. 51702057 and 11604002), the National Science Foundation (DMR 18-47701 and CER 19-11311), the Welch Foundation (E-1981), and Seed Funding for Advanced Computing (SeFAC) at the University of Houston. This research used the Maxwell/Opuntia/Sabine cluster(s) operated by the University of Houston and the Research Computing Data Core (RCDC). Support for this work was also provided by resources of the UHPC cluster managed by the University of Houston and acquired through NSF Award Number 15-31814. This work used the resources available through the 11-BM beamline at the Advanced Photon Source, an Office of Science User Facility operated for the U.S. Department of Energy (DOE) Office of Science by Argonne National Laboratory, under Contract No. DE-AC02-06CH11357.

References

1 E. F. Schubert and J. K. Kim, *Science*, 2005, **308**, 1274–1278.
2 S. Nakamura, T. Mukai and M. Senoh, *Appl. Phys. Lett.*, 1994, **64**, 1687.
3 Z. Xia and A. Meijerink, *Chem. Soc. Rev.*, 2017, **46**, 275–299.
4 G. Li, Y. Tian, Y. Zhao and J. Lin, *Chem. Soc. Rev.*, 2015, **44**, 8688–8713.
5 X. Huang, *Nat. Photonics*, 2014, **8**, 748.
6 C. C. Lin and R. S. Liu, *J. Phys. Chem. Lett.*, 2011, **2**, 1268–1277.
7 L. Chen, K. J. Chen, C. C. Lin, C. I. Chu, S. F. Hu, M. H. Lee and R. S. Liu, *J. Comb. Chem.*, 2010, **12**, 587–594.
8 J. Zhong, W. Zhao, L. Yang, P. Shi, Z. Liao, M. Xia, W. Pu, W. Xiao and L. Wang, *RSC Adv.*, 2018, **8**, 13054–13060.
9 Z. Xia, C. Ma, M. S. Molokeev, Q. Liu, K. Rickert and K. R. Poeppelmeier, *J. Am. Chem. Soc.*, 2015, **137**, 12494–12497.
10 T. Takeda, R. J. Xie, T. Suehiro and N. Hirosaki, *Prog. Solid State Chem.*, 2018, **51**, 41–51.
11 X. Wang, T. Takeda, N. Hirosaki, S. Funahashi and R. J. Xie, *J. Rare Earths*, 2018, **36**, 42–48.
12 J. Zhong, W. Zhao, F. Du, J. Wen, W. Zhuang, R. Liu, C. K. Duan, L. Wang and K. Lin, *J. Phys. Chem. C*, 2018, **122**, 7849–7858.
13 K. A. Denault, J. Brgoch, M. W. Gaultois, A. Mikhailovsky, R. Petry, H. Winkler, S. P. DenBaars and R. Seshadri, *Chem. Mater.*, 2014, **27**, 2275–2282.
14 S. Li, L. Wang, D. Tang, Y. Cho, X. Liu, X. Zhou, L. Lu, L. Zhang, T. Takeda, N. Hirosaki and R. J. Xie, *Chem. Mater.*, 2018, **30**, 494–505.
15 S. Poncé, Y. Jia, M. Giantomassi, M. Mikami and X. Gonze, *J. Phys. Chem. C*, 2016, **120**, 4040–4047.
16 R. J. Xie, N. Hirosaki, T. Suehiro, F. F. Xu and M. Mitomo, *Chem. Mater.*, 2006, **18**, 5578–5583.
17 K. Uheda, N. Hirosaki, Y. Yamamoto, A. Naito, T. Nakajima and H. Yamamoto, *Electrochem. Solid-State Lett.*, 2006, **9**, H22–H25.
18 M. Chen, Z. Xia, M. S. Molokeev and Q. Liu, *J. Mater. Chem. C*, 2015, **3**, 12477–12483.
19 Z. Tang, D. Wang, W. U. Khan, S. Du, X. Wang and Y. Wang, *J. Mater. Chem. C*, 2016, **4**, 5307–5313.
20 M. E. Huntelaar and E. H. P. Cordfunke, *J. Nucl. Mater.*, 1993, **201**, 250.
21 I. T. P. Seward, D. R. Uhlmann and D. Turnbul, *J. Am. Ceram. Soc.*, 1968, **51**, 278–285.
22 R. Zhang and P. Taskinen, *J. Alloys Compd.*, 2016, **657**, 770–776.
23 J. K. Park, M. A. Lim, K. J. Choi and C. H. Kim, *J. Mater. Sci.*, 2005, **40**, 2069–2071.
24 M. Zhang, J. Wang, Q. Zhang, W. Ding and Q. Su, *Mater. Res. Bull.*, 2007, **42**, 33–39.
25 J. Xu, Y. Zhao, J. Chen, Z. Mao, Y. Yang and D. Wang, *Luminescence*, 2017, **32**, 957–963.
26 F. Xiao, Y. N. Xue and Q. Y. Zhang, *Spectrochim. Acta, Part A*, 2009, **74**, 758–760.
27 R. Zhang, T. Maeda, R. Maruta, S. Kusaka, B. Ding, K. Murai and T. Moriga, *J. Solid State Chem.*, 2010, **183**, 620–623.
28 Q. Zhang, Q. Wang, X. Wang, X. Ding and Y. Wang, *New J. Chem.*, 2016, **40**, 8549–8555.
29 P. Wang, X. Xu, D. Zhou, X. Yu and J. Qiu, *Inorg. Chem.*, 2015, **54**, 1690–1697.
30 M. Shang, S. Liang, N. Qu, H. Lian and J. Lin, *Chem. Mater.*, 2017, **29**, 1813–1829.
31 D. Hiller, J. L. Vidrier, S. Gutsch, M. Zacharias, K. Nomoto and D. König, *Sci. Rep.*, 2017, **7**, 863.
32 X. Ji, J. Zhang, Y. Li, S. Liao, X. Zhang, Z. Yang, Z. Wang, Z. Qiu, W. Zhou, L. Yu and S. Lian, *Chem. Mater.*, 2018, **30**, 5137–5147.
33 Y. H. Kim, P. Arunkumar, B. Y. Kim, S. Unithrattil, E. Kim, S. H. Moon, J. Y. Hyun, K. H. Kim, D. Lee, J. S. Lee and W. B. Im, *Nat. Mater.*, 2017, **16**, 543–550.
34 M. Zhang, Z. Xia and Q. Liu, *J. Mater. Chem. C*, 2017, **5**, 7489–7494.
35 J. C. de Mello, H. F. Wittmann and R. H. Friend, *Adv. Mater.*, 1997, **9**, 230–232.
36 B. H. Toby, *J. Appl. Crystallogr.*, 2001, **34**, 210–213.
37 W. Kohn and L. J. Sham, *Phys. Rev.*, 1965, **140**, A1133.
38 P. Hohenberg and W. Kohn, *Phys. Rev. B: Solid State*, 1964, **136**, B864.
39 G. Kresse and J. Furthmuller, *Phys. Rev. B: Condens. Matter Mater. Phys.*, 1993, **47**, 558.
40 G. Kresse and J. Furthmuller, *Phys. Rev. B: Condens. Matter Mater. Phys.*, 1996, **54**, 11169.
41 J. Heyd and G. E. Scuseria, *J. Chem. Phys.*, 2003, **118**, 8207.
42 G. Karlström, R. Lindh, P. Malmqvist, B. O. Roos, U. Ryde, V. Veryazov, P. Widmark, M. Cossi, B. Schimmelpfennig, P. Neogrady and L. Seijo, *Comput. Mater. Sci.*, 2003, **28**, 222–239.
43 Z. Barandiarán and L. Seijo, *J. Chem. Phys.*, 1988, **89**, 5739–5746.
44 K. Andersson, P.-Å. Malmqvist, B. O. Roos, A. J. Sadlej and K. Wolinski, *J. Phys. Chem.*, 1990, **94**, 5483–5488.
45 J. Finley, P.-Å. Malmqvist, B. O. Roos and L. Serrano-Andrés, *Chem. Phys. Lett.*, 1998, **288**, 299–306.
46 B. O. Roos, P. R. Taylor and P. E. M. Siegbahn, *Chem. Phys.*, 1980, **48**, 157–173.
47 P. E. M. Siegbahn, A. Heiberg, J. Almlöf and B. O. Roos, *J. Chem. Phys.*, 1981, **74**, 2384–2396.
48 Z. Dong, Y. Qin, Y. Yang, D. Zhou, X. Xu and J. Qiu, *J. Rare Earths*, 2016, **34**, 453–457.
49 Y. Yao, Z. Zhou and F. Ye, *J. Alloys Compd.*, 2017, **712**, 213–218.
50 A. Silvestri, M. L. Ligabue, G. Malavasi and G. Lusvardi, *Materials*, 2019, **12**, 183.
51 K. F. Hesse and F. Liebau, *Z. Kristallogr. – Cryst. Mater.*, 1980, **153**, 3–18.
52 D. Cao, H. Wang, H. Wei and W. Yang, *J. Semicond.*, 2015, **36**, 123008.
53 I. Cho, D. K. Yim, C. H. Kwak, J. S. An, H. S. Roh and K. S. Hong, *J. Lumin.*, 2012, **132**, 375–380.

54 Z. Xia and R. S. Liu, *J. Phys. Chem. C*, 2012, **116**, 15604–15609.
55 G. Blasse and B. C. Grabmaier, *Luminescent Materials*, Springer, Berlin, 1994.
56 T. Katsumata, T. Nabae, K. Sasajima, S. Komuro and T. Morikawa, *J. Electrochem. Soc.*, 1997, **144**, L243–L245.
57 Y. Zheng, W. Zhuang, X. Xing, J. Zhong, R. Liu, Y. Li, Y. Liu and Y. Hu, *RSC Adv.*, 2016, **6**, 68852–68859.
58 Y. Li, Y. Wang, X. Xu, G. Yu and N. Wang, *J. Am. Ceram. Soc.*, 2011, **94**, 496–500.
59 J. Zhong, W. Zhuang, X. Xing, L. Wang, Y. Li, Y. Zheng, R. Liu, Y. Liu and Y. Hu, *J. Alloys Compd.*, 2016, **674**, 93–97.
60 A. C. Duke, S. Hariyani and J. Brgoch, *Chem. Mater.*, 2018, **30**, 2668–2675.
61 F. Urbach, *Cornell Symposium*, Wiley, New York, 1948.